Oxygen vacancy induced photoconductivity enhancement in $Bi_{1-x}Ca_xFeO_{3-\delta}$ nanoparticle ceramics: A combined experimental and theoretical study

Subhajit Nandy, Kulwinder Kaur, Pavana S. V. Mocherla, B. R. K. Nanda, and C. Sudakar

Citation: Journal of Applied Physics **124**, 195108 (2018); doi: 10.1063/1.5055742
View online: https://doi.org/10.1063/1.5055742
View Table of Contents: http://aip.scitation.org/toc/jap/124/19
Published by the American Institute of Physics

JOURNAL OF APPLIED PHYSICS **124**, 195108 (2018)

Oxygen vacancy induced photoconductivity enhancement in $Bi_{1-x}Ca_xFeO_{3-\delta}$ nanoparticle ceramics: A combined experimental and theoretical study

Subhajit Nandy,[1] Kulwinder Kaur,[2] Pavana S. V. Mocherla,[1] B. R. K. Nanda,[2] and C. Sudakar[1,a)]

[1]*Multifunctional Materials Laboratory, Department of Physics, Indian Institute of Technology Madras, Chennai 600 036, India*

[2]*Condensed Matter Theory and Computational Laboratory, Department of Physics, Indian Institute of Technology Madras, Chennai 600 036, India*

(Received 10 September 2018; accepted 2 November 2018; published online 20 November 2018)

Based on experimental and density functional studies, we show that tailoring of oxygen vacancies (O_V) leads to large scale enhancement of photoconductivity in $BiFeO_3$ (BFO). The O_V concentration is increased by substituting an aliovalent cation Ca^{2+} at Bi^{3+} sites in the BFO structure. Furthermore, the O_V concentration at the disordered grain boundaries can be increased by reducing the particle size. Photoconductivity studies carried out on spark plasma sintered $Bi_{1-x}Ca_xFeO_{3-\delta}$ ceramics show four orders of enhancement for $x = 0.1$. Temperature dependent Nyquist plots depict a clear decrease in impedance with increasing Ca^{2+} concentration which signifies the role of O_V. A significant reduction in photoconductivity by 2 to 4 orders and a large increase in impedance of the air-annealed (AA) nanocrystalline ceramics suggest that O_V at the grain boundaries primarily control the photocurrent. In fact, activation energy for AA samples (0.5 to 1.4 eV) is larger than the as-prepared (AP) samples (0.1 to 0.5 eV). Therefore, the room temperature J-V characteristics under 1 sun illumination show 2–4 orders more current density for AP samples. Density-functional calculations reveal that, while the defect states due to bulk O_V are nearly flat, degenerate, and discrete, the defect states due to surface O_V are non-degenerate and interact with the surface dangling states to become dispersive. With large vacancy concentration, they form a defect band that enables a continuous transition of charge carriers leading to significant enhancement in the photoconductivity. These studies reveal the importance of tailoring the microstructural features as well as the composition-tailored properties to achieve large short circuit current in perovskite oxide based solar cells. *Published by AIP Publishing.* https://doi.org/10.1063/1.5055742

I. INTRODUCTION

$BiFeO_3$, known for its above room temperature multiferroic properties, is now capturing attention for its potential application as a photoferroelectric material.[1–3] The idea of exploring ferroelectric oxides for photovoltaic applications was long-proposed, however, special interest in $BiFeO_3$ surged after a recent article by Yang *et al.*[4] showing a large photovoltage of 33 V in (001) oriented $BiFeO_3$ thin films. Bhatnagar *et al.* have shown an enhanced photovoltage (to ~50 V) via controlling domain wall conductivity.[5] $BiFeO_3$ also has the advantage of least bulk bandgap among all the other ferroelectric materials (E_g ~2.5 eV).[6] Several reports established easy bandgap tuning of $BiFeO_3$ in various morphological[7] and microstructural[8] configurations and the lowest value of 2.1 eV has been reported.[8] Besides the merits of producing large photovoltages and good photoabsorption due to small bandgap, a proper photoferroelectric requires to be tested for its carrier recombination and photocurrent response which depend largely on the stoichiometry of a compound. $BiFeO_3$ is known for its narrow thermal stability[9] and is highly prone to anionic (oxygen vacancies, O_V) and cationic defects (Bi and Fe vacancies, Bi_V and Fe_V).[10] While oxygen rich conditions promote Bi_V and Fe_V as dominant cationic defects, O_V and Bi_V dominate in oxygen deficient conditions.[10] The influence of defects becomes more pronounced at nanoscale, where the surface area to volume ratio is much higher compared to that of bulk. Several studies demonstrate the effect of oxygen vacancies and resulting strain on structural, magnetic, optical, electrical, and magnetoelectric properties of $BiFeO_3$.[1,11–14] Conventionally, oxygen vacancies are believed to be the primary source of electric leakage in $BiFeO_3$ and efforts were made to eliminate these for better physical property variation.[15] According to local density approximation studies carried out by Clark and Robertson,[16] oxygen vacancies in $BiFeO_3$ act predominantly as double donors with an effective charge of +2 besides possible states of 0 and +1. These levels are estimated to be lying just 0.6 eV below the conduction band confirming them as primary leakage sources.[16] On the other hand, a few experimental studies suggested that oxygen vacancies can be used as a tool to improve optical and magnetic properties of $BiFeO_3$ for device applications.[8,17,18] However, understanding the influence of these vacancies and altered stoichiometry on photoconductivity of $BiFeO_3$ requires a thorough analysis of a material at nanoscale where the defect concentration is larger. Oxygen vacancies can be easily incorporated into a lattice by substituting cation sites with aliovalent dopants. Ca^{2+} (114 pm) doping at Bi^{3+} (117 pm) site is a preferred case

a)Author to whom correspondence should be addressed: csudakar@iitm.ac.in

due to the close match in their ionic sizes as well as due to the attractive optical properties reported earlier.[1,17] It is shown that the bandgap can be brought down to 1.5 eV in Ca doped $BiFeO_3$ by optimizing size, strain, and annealing conditions.[8] Kianinia *et al.* reported ten times higher dark conductivity in Ca doped $BiFeO_3$ compared to phase-pure $BiFeO_3$.[2] Formation of *n-p* junction by the migration of oxygen vacancies under electric field in Ca doped $BiFeO_3$ thin films was also reported by Bharathi *et al.*[19] Furthermore, enhancement of conductivity and resistive switching in bulk Ca doped $BiFeO_3$ was discussed in detail by Maso *et al.*[20,21] The dependence of photoconductivity on oxygen vacancies was also reported in other oxide systems.[22] Photon induced conductance enhancement from 3.2×10^{-6} S to 4×10^{-6} S due to oxygen vacancy was demonstrated on vacuum annealing in $La_{0.5}Sr_{0.5}CoO_{3-\delta}$, which introduces significant oxygen deficiency with respect to stoichiometric perovskite $La_{0.5}Sr_{0.5}CoO_3$.[22] Our previous studies on spark plasma-sintered phase-pure BFO revealed a significant influence of morphology and oxygen vacancies on the photoconductivity response. Vacancies present on the nanoparticle surfaces act as a major conducting channel for photocarriers.[23]

In this paper, we discuss the prominent role of oxygen vacancies introduced via Ca^{2+} doping at Bi^{3+} site and those residing on the nanoparticle surfaces in controlling the photoconductivity. To obtain densely packed nanoparticles for the photoconductivity measurement, spark plasma sintered (SPS) pellets were fabricated. The influence of oxygen vacancies on the conduction properties of as prepared $Bi_{1-x}Ca_xFeO_{3-\delta}$ ($x=0$, 0.05, 0.1) pellets is discussed using the frequency-dependent impedance spectroscopy measurements. Air annealing conditions that alter the grain boundary conductivity are revealed, and its influence on the photoconductivity is discussed. We show that, while the oxygen vacancies present in the grains are essential to improve photoconductivity, the grain boundary conductivity controlled in turn by the oxygen stoichiometry is also significant for observing the enhanced photoconductivity in $Bi_{1-x}Ca_xFeO_{3-\delta}$. A large increase in photoconductivity response by 4 orders of magnitude is observed in 10 at. % Ca^{2+} doped BFO samples, establishing the substantial role of oxygen vacancies in aiding the photoconduction process. The density-functional calculations are carried out to examine the formation of vacancy-induced defect states and their contribution to the photoconductivity response.

II. EXPERIMENTAL

$Bi_{1-x}Ca_xFeO_{3-\delta}$ nanoparticles were prepared by the low temperature citrate sol-gel process.[8] In a typical preparation of $Bi_{1-x}Ca_xFeO_{3-\delta}$, $Bi(NO_3)_3{\cdot}5H_2O$, $Fe(NO_3)_3{\cdot}9H_2O$, and $CaCl_2{\cdot}2H_2O$ are taken in an appropriate mole ratio and dissolved in deionized water to obtain 0.2M solutions of each. A small amount of dilute HNO_3 was added to obtain a clear solution. All these solutions are mixed and an anhydrous citric acid is added to the final solution in 1:1 ratio with metal cations. This mixture is stirred continuously to obtain a homogeneous gel by heating on a hot plate at 80 °C. It is further heated at 100 °C till the gel completely gets dried and becomes coarse powder. This precursor powder was ground well and calcined at 550 °C for 1 h in air. These calcined powders were made into dense pellets of 20 mm diameter in a graphitic die using spark plasma sintering (SPS) technique. An optimum pressure of 40 MPa and a temperature of 650 °C were applied for 5 min during the sintering process to minimize rapid grain growth. Three samples were prepared via SPS technique: (i) $BiFeO_3$ (BFO; $x=0$), (ii) $Bi_{0.95}Ca_{0.05}FeO_{3-\delta}$ (BC5FO; $x=0.05$), and (iii) $Bi_{0.9}Ca_{0.1}FeO_{3-\delta}$ (BC10FO; $x=0.1$). These sintered pellets were polished to eliminate graphitic carbon induced into the pellets from the die during sintering. The as-prepared (AP) pellets were annealed at 550 °C for 15 min in air ambient to allow diffusion of oxygen vacancies (O_V). These pellets are referred to as air-annealed (AA) pellets. All the characterization and corresponding analysis presented henceforth is discussed comparatively between AP and AA SPS pellets.

III. RESULTS AND DISCUSSION

A. Experimental studies on $Bi_{1-x}Ca_xFeO_{3-\delta}$ ($x=0$, 0.05, 0.1)

Figure 1 shows the x-ray diffraction (XRD) data of as-prepared BFO (BFO-AP) and air-annealed BFO (BFO-AA) pellets of $Bi_{1-x}Ca_xFeO_{3-\delta}$ ($x=0$, 0.05, 0.1) recorded on a Rigaku diffractometer with a Cu-Kα source ($\lambda=1.5406$ Å). All the peaks in the diffraction patterns were indexed with respect to a standard pattern of $BiFeO_3$ (ICDD file #71-2494) with a rhombohedral structure (R3c space group). A small percentage of secondary phase $Bi_2Fe_4O_9$ is found in BFO-AP and BFO-AA. As-prepared (BCFO-AP) and air-annealed (BCFO-AA) Ca doped samples show $Bi_2Fe_4O_9$ and Fe_2O_3 in small quantities. The presence of secondary phases in small fraction is unavoidable in nanopowders and sintered pellets of bismuth ferrite due to its narrow thermal stability in the phase diagram.[9] These secondary phases are usually prominent in samples annealed at higher temperature (>650 °C). High local temperatures produced during the plasma sintering make it

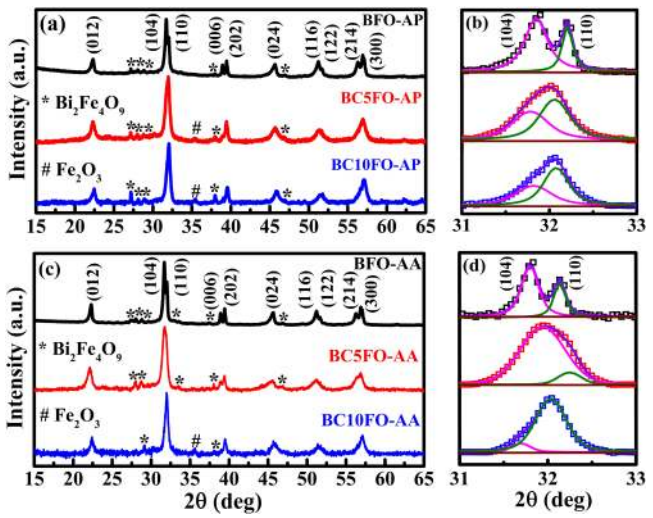

FIG. 1. X-ray diffraction patterns of [(a) and (b)] as-prepared (AP) and [(c) and (d)] air annealed (AA) $Bi_{1-x}Ca_xFeO_{3-\delta}$ ($x=0$, 0.05, 0.1) SPS pellets (BFO, BC5FO, and BC10FO correspond to $x=0$, 0.05, and 0.1, respectively).

difficult to avoid the secondary phases in the SPS pellets. Both as-prepared BFO (BFO-AP) and air-annealed BFO (BFO-AA) show clear splitting of (104) and (110) double peak indicating good crystallinity of the samples. A reduction in the separation between double peaks is discerned with increasing Ca concentration. For BC5FO and BC10FO, (104) and (110) peaks merge into a single peak with the intensity of (104) reflection decreasing relative to (110) reflection. This implies a structural transformation from the rhombohedral distortion to orthorhombic phase.[24] Such structural changes clearly result from the substitutional effect of Ca at Bi sites.[17]

Raman spectra on AP and AA pellets of $Bi_{1-x}Ca_xFeO_{3-\delta}$ ($x = 0$, 0.05, 0.1) were acquired using a 632 nm excitation from the He-Ne laser of a Horiba-Jobin Yvon spectrometer at room temperature (Fig. 2). Multiple acquisitions from 100 to 700 cm^{-1} for a time of 60 s each were collected on the pellets at different positions. The spectra obtained from various regions are similar. All the spectra showed a total of 13 modes ($4A_1$+9E) corresponding to the rhombohedral structure,[25] with a slight shift and broadening observed in the modes. It is reported that the low frequency E(TO) (<200 cm^{-1}) modes correspond to Bi centered activity Bi-O bonds and high frequency modes are dominated by Fe-O vibrational features.[14,26,27] Two intense peaks, around 138 cm^{-1} and 170 cm^{-1} corresponding to Bi-O vibrational E(TO) modes, were observed in BFO-AP and BFO-AA.[25] These modes become broader and diffuse with the introduction of Ca^{2+} at Bi^{3+} site in BCFO-AP. These modes are seen to be well-defined in BCFO-AA; however, a small blue-shift from 138 cm^{-1} to 143 cm^{-1} is observed. Introduction of an aliovalent Ca^{2+} cation of smaller ionic size (r = 114 pm) alters the occupancy of Bi^{3+} (r = 117 pm) ions within the unit cells. Since phonon frequency is an inverse function of mass, Ca-O activity results in an increased blue shift of Raman frequencies with increasing Ca^{2+} in the samples.[28,29] The characteristic two phonon mode of $BiFeO_3$ centered around 1200 cm^{-1} is analyzed as a function of doping concentration. For single-phase bulk $BiFeO_3$, this mode comprises three peaks at ~969, 1088, and 1271 cm^{-1} corresponding to the overtones of fundamental Fe-O vibrations at ~476, 558, and 650 cm^{-1}.[18,29] Peaks at 969 cm^{-1} and 1271 cm^{-1} are shifted to higher frequencies in all cases, indicating the influence of Ca doping and resulting local strains on the Bi-O and Fe-O bond configurations [Figs. 2(b) and 2(d)]. Gradual modification of rhombohedral double peak in XRD and Raman modes confirms the doping of Ca at Bi site in BCFO pellets. Field emission scanning electron microscopy (FESEM) images of SPS pellets are shown in Fig. 3. BFO-AP showed a mixed morphology of large grains (1 to 2 μm) and nanoparticles of size 100 to 200 nm located along the grain boundaries. On air-annealing BFO-AP sample for 15 min, the nanoparticles residing at the grain boundaries coalesce with larger grains. The morphology of BFO-AA is more uniform with well-defined grain boundaries devoid of any nanoparticles. Nevertheless, the average size of larger grains in both BFO-AP and BFO-AA remains almost the same. In BCFO (5 at. %) pellets, grain size decreases by an order. With further increase in Ca concentration to 10 at. %, grains lose their faceted appearance and become agglomerated spheres. Average grain sizes are found to be ~200 nm for BC5FO-AP and ~100 nm for BC10FO-AP. Air-annealing does not seem to have much influence on the grain morphology or size of the Ca doped BFO samples. The average grain size for BC5FO-AA and BC10FO-AA remains to be ~200 nm and ~100 nm, respectively.

In order to evaluate the differences that arise in the electrical characteristics of BFO and BCFO samples post air-annealing, we carried out temperature-dependent impedance analysis (123 K to 573 K with an interval of 15 K) on all samples using a dielectric resonance spectrometer (Novocontrol Technologies) in a capacitor configuration within the frequency range 100 Hz to 40 MHz. Figure 4 shows the Nyquist plots (Z′ vs.−Z″) in the range 453 K to 573 K, to highlight the important changes at high temperature, for all AP and AA samples. The set of data from 303 K to 573 K is given in Fig. S1 in the supplementary material. It is observed that the

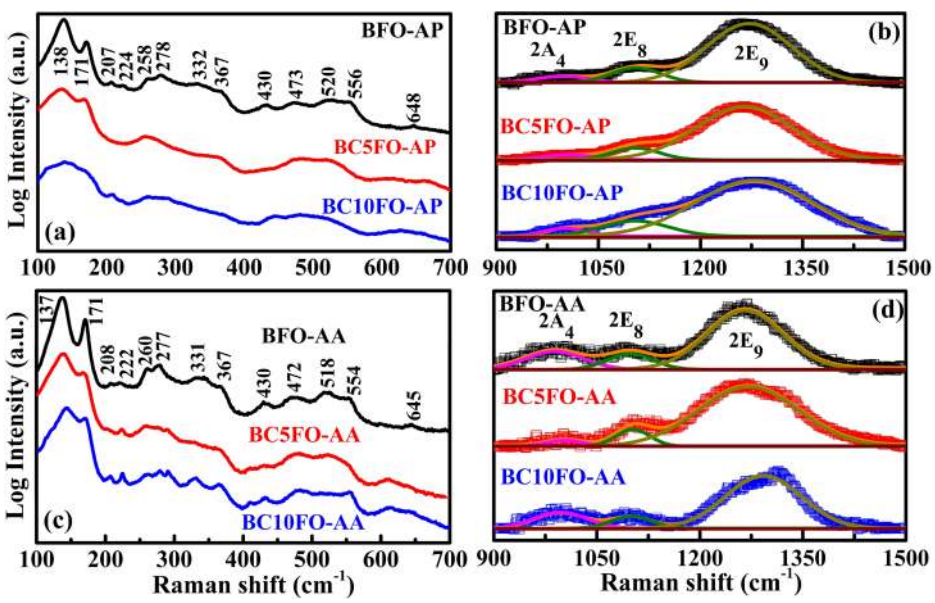

FIG. 2. Raman spectra of [(a) and (b)] as-prepared (AP) and [(c) and (d)] air annealed (AA) $Bi_{1-x}Ca_xFeO_{3-\delta}$ ($x = 0$, 0.05, 0.1) SPS pellets (BFO, BC5FO, and BC10FO correspond to $x = 0$, 0.05, and 0.1, respectively).

room temperature impedance (Z′) starts to decrease with increasing temperature for all the samples, indicating an increase in conductivity. BFO-AA showed higher impedance than BFO-AP at all temperatures. An additional contribution identified in the Nyquist plot of BFO-AP [Fig. 4(a)] at high temperature shows the contribution from nanoparticles residing along the grain boundaries.[23] The absence of similar contribution in BFO-AA sample further confirms the active role of nanoparticles at the grain boundaries in BFO-AP sample. Ca doping in BFO showed a drastic reduction in impedance value compared to pure BFO. BC5FO-AP and BC10FO-AP samples showed reduced impedance by almost three and four orders, respectively, compared to BFO-AP. A systematic decrease in impedance of BCFO-AP with increasing Ca^{2+} confirms the role of oxygen vacancies in modifying electrical properties. On the other hand, BC5FO-AA and BC10FO-AA samples show an increase in impedance by two and three orders of magnitude, respectively, compared to their AP counterparts. This change is attributed to the suppression of oxygen vacancies situated on the surface or grain boundaries during air-annealing. However, the impedance profiles of BCFO-AA show slightly smaller values compared to BFO-AA, suggesting that these samples are not completely devoid of oxygen vacancies. BCFO-AA samples contain oxygen vacancies within the particle cores due to the aliovalent doping even after air-annealing.

The imaginary part of impedance Z″ as a function of frequency is shown in Fig. 5. The plots shown in these figures correspond to the data given in Fig. 4. BFO-AP showed a single peak around 2 kHz at 303 K (Fig. S2 in the supplementary material). This peak shifts to a higher frequency as the measurement temperature is increased. The asymmetric shape of the peaks indicates multiple relaxation processes and non-Debye type behavior in the system.[30] With increase in temperature above 303 K, we see that the peak profile consists of an additional second peak. Above 453 K, a third peak emerges on the lower frequency side (10^2 to 10^3 Hz) (Fig. 5). At room temperature, different contributions to the total impedance are not well-resolved and they become apparent only at high temperature. The observed peaks are attributed to the grain boundary (10^2 to 10^3 Hz), nanoparticle (10^4 to 10^5 Hz), and grain relaxations (>10^5 Hz) similar to those evidenced from the Nyquist plots. The peak seen at intermediate frequencies is attributed to the conduction due to nanoparticles available at the grain boundaries in BFO-AP.[23] By contrast, BFO-AA displayed a much higher impedance profile

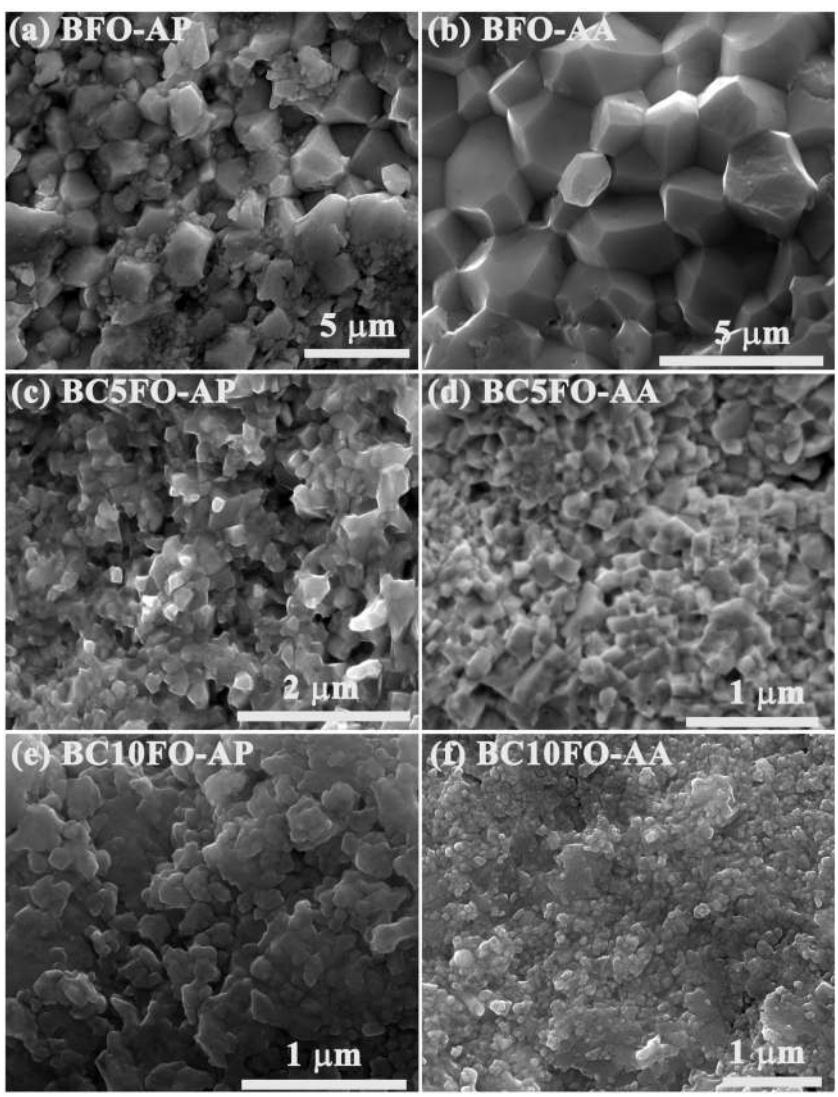

FIG. 3. FESEM images of [(a), (c), and (e)] as prepared (AP) and [(b), (d), and (f)] air annealed (AA) $Bi_{1-x}Ca_xFeO_{3-\delta}$ ($x = 0$, 0.05, 0.1) SPS pellets (BFO, BC5FO, and BC10FO correspond to $x = 0$, 0.05, and 0.1, respectively).

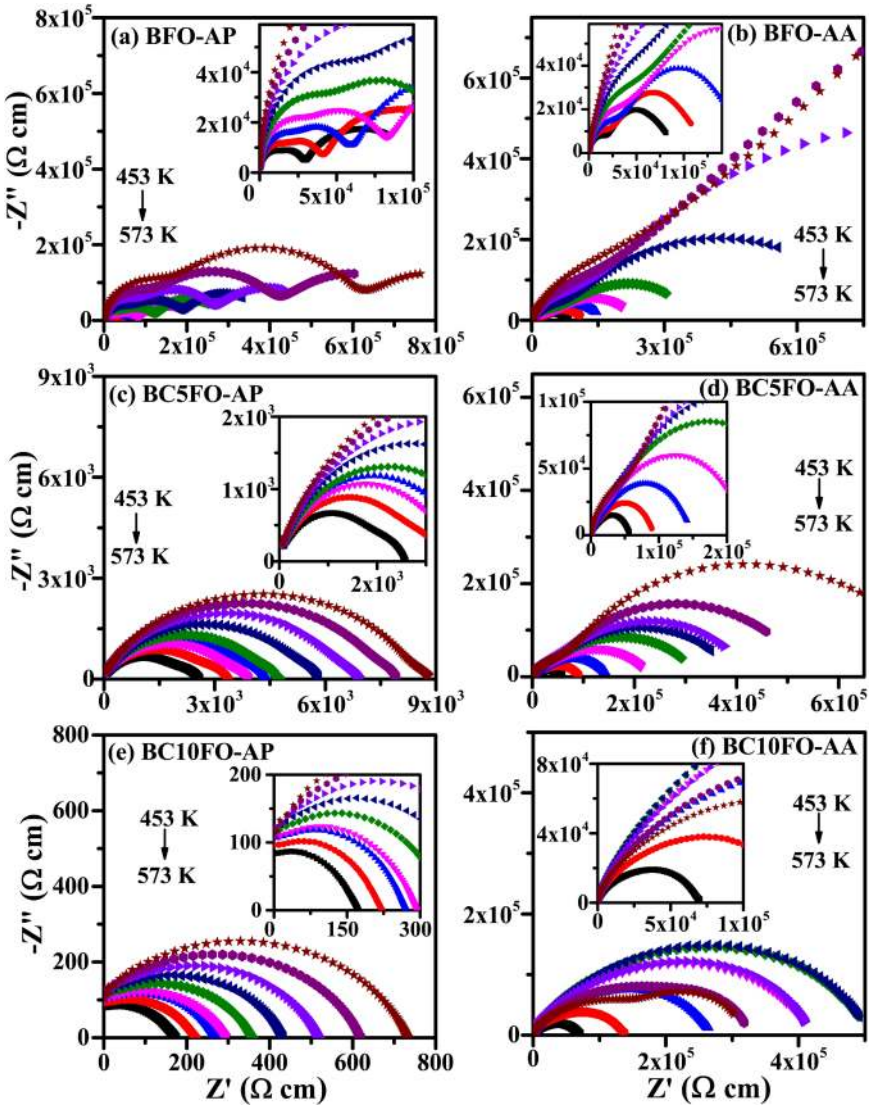

FIG. 4. Nyquist plots of [(a), (c), and (e)] as-prepared (AP) and [(b), (d), and (f)] air annealed (AA) $Bi_{1-x}Ca_xFeO_{3-\delta}$ ($x = 0$, 0.05, 0.1) pellets measured in the temperature range of 453 K to 573 K. The data are acquired at the temperature intervals of 15 K (BFO, BC5FO, and BC10FO correspond to $x = 0$, 0.05, and 0.1, respectively).

with its relaxation peak visible only above 513 K. This sample shows only two contributions to the overall impedance, i.e., grain (at high frequencies) and grain boundary (at low frequencies). Lack of third relaxation peak in BFO-AA as in the case of BFO-AP confirms the nanoparticle origin of this peak in BFO-AP. BC5FO-AP initially showed a single symmetric relaxation peak centered at 10^5 to 10^6 Hz at room temperature (Fig. S2 in the supplementary material). With increase in temperature, we observed an asymmetric shift in the impedance profile toward high frequencies particularly for those data recorded above 453 K. This indicates the divergence of the second relaxation process at higher temperatures. On the other hand, BC5FO-AA showed four orders of enhanced impedance loss compared to BC5FO-AP with no relaxation peak observed in the measured range till 483 K. This peak identified above 483 K is seen shifting to higher frequencies with further increase in temperature.

It is interesting to note that the relative impedance loss values of the grain and grain boundary relaxation peaks in BC5FO-AP reverse in BC5FO-AA. This suggests that the oxygen vacancies present at the grain boundaries participate more in conduction than those inside the grains in BC5FO-AP. On suppressing these vacancies by air-annealing in BC5FO-AA, the boundaries get more resistive compared to the grains. Likewise, BC10FO-AP sample showed impedance characteristics with single relaxation peak but positioned relatively at higher frequency range 10^6 to 10^7 Hz. However, with increase in temperature, the peak maxima shift beyond 10^7 Hz making it difficult to look for resolved features. BC10FO-AA also showed an increase in impedance loss by four orders with some anomalies above 453 K. At this temperature, we see that the peak between 10^3 and 10^5 Hz becomes unusually dominant than the one present at lower frequencies. The overall profile at high temperatures for this sample shows discontinuities in terms of peak shifts we normally observed in other samples, limiting us to analyze their temperature dependence.

The imaginary component of impedance Z″ vs frequency plots is curve fitted with Gaussian profiles to de-convolute for exact peak positions in each case. A representative plot at 573 K with the fitted peaks is shown in Fig. S3 in the supplementary material. The activation energy (E_a) associated with a relaxation process is obtained from the slope of ln ω vs. 1/T plots (Fig. 6) according to the Arrhenius equation $\ln\omega = \ln\omega_0 - \frac{E_a}{k_B T}$, where $\omega = 2\pi f$, f is the relaxation frequency of the peak, k_B is the Boltzmann constant, and

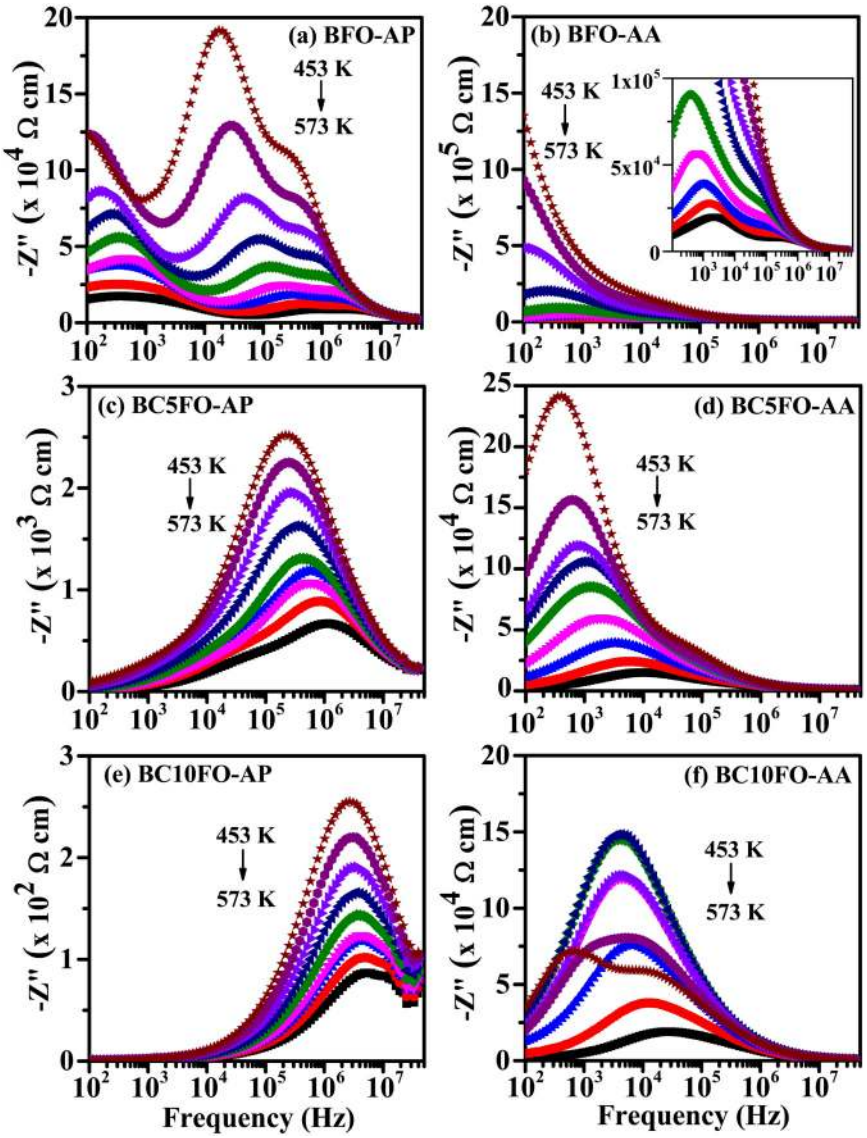

FIG. 5. Frequency response of imaginary part of impedance [(a), (c), and (e)] for as-prepared (AP) and [(b), (d), and (f)] for air annealed (AA) $Bi_{1-x}Ca_xFeO_{3-\delta}$ ($x = 0$, 0.05, 0.1) pellets measured in the temperature range of 453 K to 573 K. The data are acquired at temperature intervals of 15 K (BFO, BC5FO, and BC10FO correspond to $x = 0$, 0.05, and 0.1, respectively).

T is temperature in Kelvin. Activation energy plots corresponding to the individual relaxation mechanisms are plotted in Fig. 6, and their values are listed in Table I. The activation energies decrease with increasing Ca concentration in both AP and AA samples. It is also seen that all the activation energy values of AP samples corresponding to the grain and grain-boundary conductions show an increased value in AA samples. This clearly confirms the role of oxygen vacancies in aiding the conduction process in as-prepared SPS pellets. Reduction in these vacancies after air-annealing makes the conduction difficult resulting in large activation energies. It is well-known that O_V adopt different migratory patterns depending on the concentration and correlation among them. If the number of O_V is sufficient enough, they migrate collectively with minimum activation energy and individual motion is dominated as they reduce in number. The energy required to initiate individual motion of these vacancies is always higher than that of collective migration.[31] It is shown that for a stoichiometric perovskite of ABO_3, the activation energy is around 2 eV and reduces as the O_V is increased.[32] It has also been reported that the activation energy is in the range of 0.4–0.5 eV for singly ionized O_V, whereas it lies in between 0.6 and 1.2 eV for doubly ionized O_V in ferroelectric perovskite systems like $BaTiO_3$ or $PbTiO_3$.[33] Now, if a material is intrinsically rich of vacancies like in our BCFO samples, we expect much smaller activation energies ($E_a < 1$ eV).[30] These values not only depend on concentration but also on the position of these vacancies. If there is a clustering of vacancies in the pellets, it is easy for the collective migration to take place regardless of the number of vacancies present.

Arrhenius plots of temperature dependent *ac* conductivity measured at a frequency of 100 Hz are shown for both AP and AA samples in Fig. 7. An increase in *ac* conductivity was observed for both AP and AA samples with increasing temperature. A remarkable reduction in conductivity is observed with air-annealing for all the samples. A linear dependence with different slopes over a wide range of temperature from 123 K to 573 K is observed. Three regions of conductivity variation (marked by dotted lines in the Fig. 7), (i) R_1 from 363 K to 573 K, (ii) R_2 from 183 K to 348 K, and (iii) R_3 from 123 K to 168 K, indicate three transport mechanisms in these pellets. In general, high temperature conduction in $Bi_{1-x}Ca_xFeO_{3-\delta}$ is attributed mostly to the ionic contribution, and at room temperatures, it is accounted to the

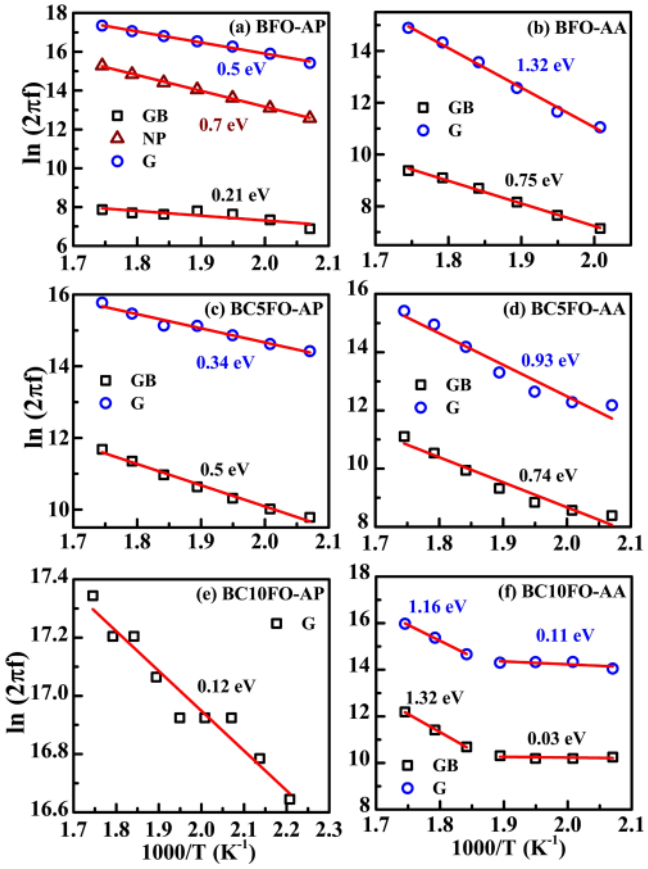

FIG. 6. Arrhenius plots of [(a), (c), and (e)] as-prepared (AP) and [(b), (d), and (f)] air annealed $Bi_{1-x}Ca_xFeO_{3-\delta}$ ($x = 0$, 0.05, 0.1) pellets measured in the temperature range of 453 K to 573 K. Open symbols show the measured data point, and solid line is the linear fit (BFO, BC5FO, and BC10FO correspond to $x = 0$, 0.05, and 0.1, respectively).

charge transport through electron and hole hopping (called polaronic conduction).[30] In our case, at high temperature (region R_1), activation energies ranging from 0.18 eV to 0.36 eV for AP pellets and 0.4 eV to 0.44 eV for AA pellets can be attributed to the O_V related ionic conduction at the grain boundaries. Increase in the activation energies of region R_1 in AA pellets than those observed in AP pellets clearly suggests the reduction of O_V related conduction at the grain boundaries. The activation energy in region R_1 is higher for BFO-AP (0.36 eV) than that of doped samples (~0.2 eV), confirming the role of O_V in causing conduction. Activation energies in regions R_2 and R_3 can be associated with

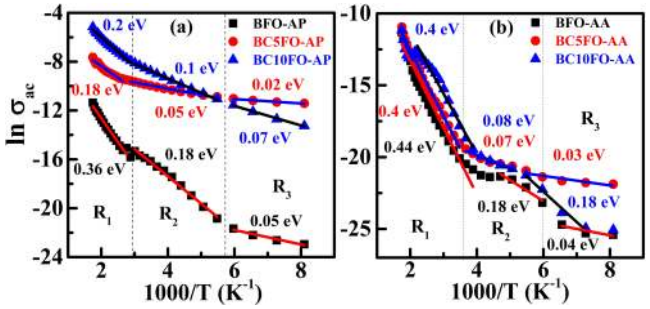

FIG. 7. AC conductivity vs. 1000/T plots at 100 Hz frequency for (a) as-prepared (AP) and (b) air annealed (AA) $Bi_{1-x}Ca_xFeO_{3-\delta}$ ($x = 0$, 0.05, 0.1) pellets. Symbols show the measured data point, and solid line is the linear fit (BFO, BC5FO, and BC10FO correspond to $x = 0$, 0.05, and 0.1, respectively).

polaronic conduction. These conductivity curves show modified slopes for AA samples where the region R_1 extends down to almost 260 K, i.e., close to room temperature. The region R_2 narrows down with air-annealing while R_3 is unaltered. Activation energy values of AP and AA samples are listed in Table II.

The J-V characteristics (Fig. 8) and photoconductivity measurements (Fig. 9) were done on the pellets using the van der Pauw four-probe method. Silver point contacts were made at the edges of the pellets connected with thin copper wires. The area and thickness of the pellets used for the photoconductivity measurements are roughly ~0.25 cm^2 and ~1 mm, respectively. J-V curves were obtained under the dark and illuminated conditions of AM 1.5 one sun light source (100 mW/cm^2) from the solar simulator. For photoconductivity measurements, a constant current using a Keithley (model 2400) current-source meter is applied and the resistance is measured by monitoring the voltage as a function of time under ON and OFF conditions. For brevity, the measured conductivity is plotted vs. time for three cycles (Fig. 9). J-V curves (Fig. 8) show 2 to 3 times increase in current density on exposing the samples with light. A dark current density of 10^{-5} A/cm^2 is observed at 20 V for BFO-AP, whereas BFO-AA showed 10^{-7} A/cm^2 dark current at the same voltage. Two orders of more dark current in BFO-AP can be attributed to the lower resistivity of these samples compared to the BFO-AA. In the case of BFO-AP, the current obtained during the exposure of light is more than dark current for the whole voltage range in the J-V plot. However, this is found to be contrary for BFO-AA sample where the current density

TABLE I. Activation energy values from ln (2πf) vs 1000/T plot (GB, grain boundary; NP, nanoparticle). The values given in the parenthesis correspond to fit for high temperature (483 K to 528 K).

	Activation energy (eV)				
	AP			AA	
Sample	Grain	GB	NP	Grain	GB
BFO	0.5	0.21	0.7	1.32	0.75
BC5FO	0.34	0.5	…	0.93	0.74
BC10FO	0.12	…	…	1.16 (0.11)	1.32 (0.03)

TABLE II. Activation energy values from σ_{ac} vs 1000/T plot of all as-prepared (AP) and air-annealed (AA) pellets.

	Activation energy (eV)					
	AP			AA		
Sample	R_1	R_2	R_3	R_1	R_2	R_3
BFO	0.36	0.18	0.05	0.44	0.18	0.04
BC5FO	0.18	0.05	0.02	0.40	0.07	0.03
BC10FO	0.20	0.10	0.07	0.40	0.08	0.18

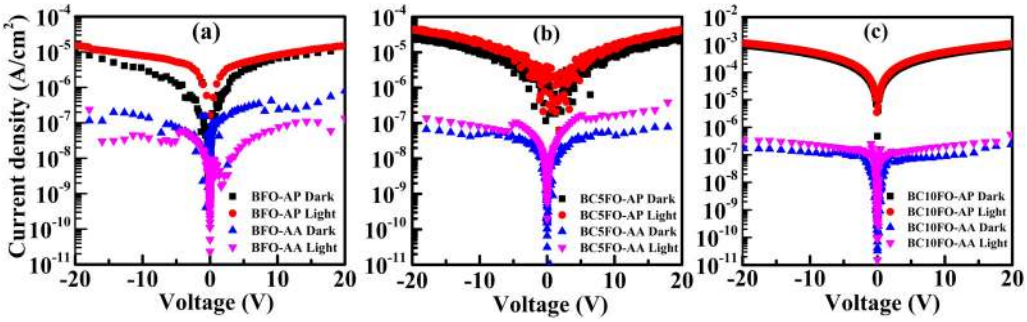

FIG. 8. Current density vs voltage (J-V) characteristics of (a) BFO, (b) BC5FO, (c) BC10FO as-prepared (AP) and air-annealed (AA) pellets under the ON and OFF conditions of 1 sun illumination.

on exposure to light decreases by 3 times compared to dark current density. Thus, while both samples showed a clear photoresponse on exposure to light, BFO-AP showed an increased conductivity under illumination, whereas the current drops for BFO-AA. This trend is also reflected in the conductivity vs time plots obtained under the ON and OFF state of AM 1.5 source [Figs. 9(a) and 9(b)]. In BFO-AP, the conduction channels due to the surface oxygen vacancies on the nanoparticles present at the grain boundaries resulted in larger photoconductivity.[23] Whereas in BFO-AA, the absence of surface conduction channels along with the dominant role played by photoinduced traps resulted in decreased conductivity on illumination.[23]

With Ca doped samples, BC5FO-AP and BC10FO-AP, the dark current density is found to be one to two orders of magnitude more compared to that observed for pure BFO-AP

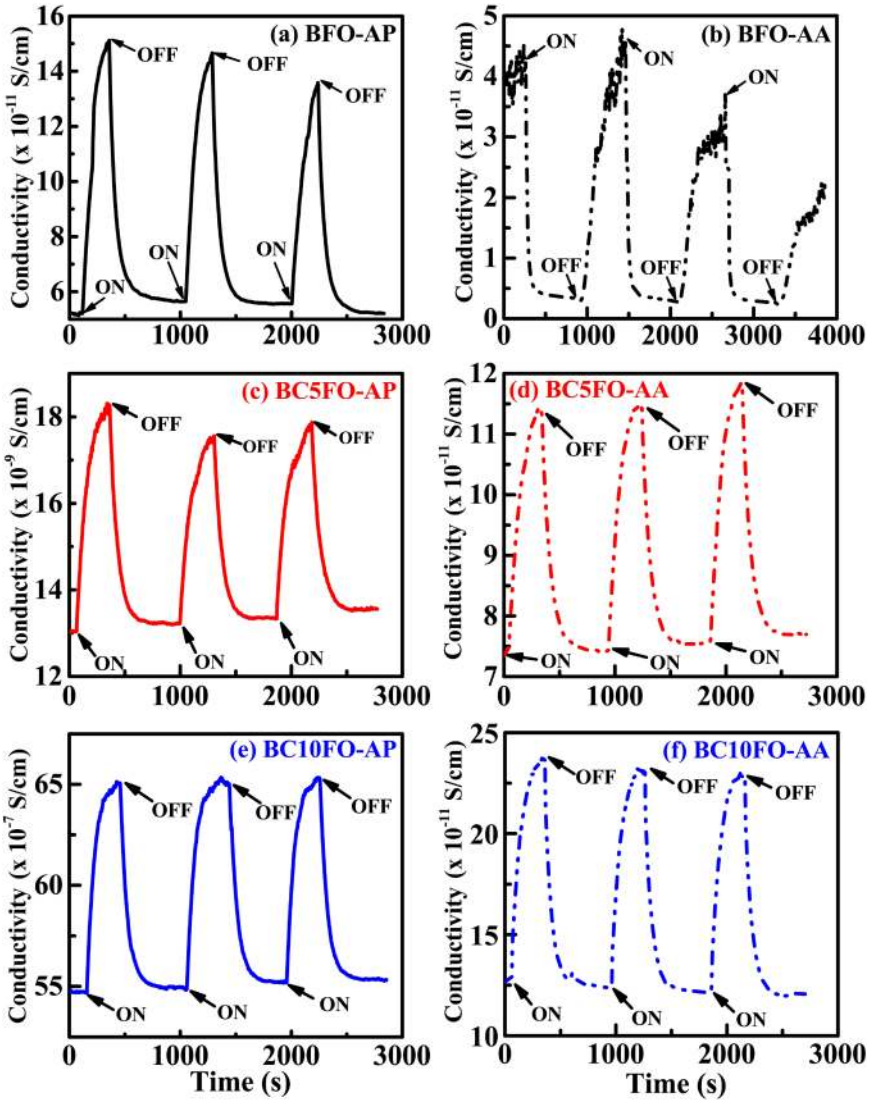

FIG. 9. Conductivity vs. time plots of all as-prepared [(a) BFO, (c) BC5FO, and (e) BC10FO] and air-annealed [(b) BFO, (d) BC5FO, and (f) BC10FO] samples with 1 sun illuminating light ON and OFF conditions.

samples. This observation also agrees with the reports showing the highest enhancement of conductivity occurring in 10% to 15% Ca doped $BiFeO_3$ thin films[2] and ceramics.[34] On illumination with AM 1.5 light, roughly onefold to twofold increase in current density is observed. For the BC5FO-AA sample, the dark current density is two orders lower than BC5FO-AP. This trend is also seen in BC10FO-AA, where three orders of lower dark current than BC10FO-AP is found. It is interesting to note the report by Maso *et al.*[21] who have demonstrated that depending on the oxygen partial pressure used during the processing, the conductivity of Ca-doped $BiFeO_3$ ceramics varies by many orders of magnitude. Thus, all AA samples showed two to three orders of lower dark current than their corresponding AP samples. This is consistent with the higher resistivity of AA samples observed from the Nyquist plots.

The photoconductivity measurements of BC5FO and BC10FO are shown in Fig. 9. On illumination, conductivity increased exponentially and saturated after ~5 min. On stopping the illumination, conductivity returned to initial values with an exponential decay. The change in conductivity is about 1×10^{-10} S/cm for BFO-AP, which increases to 5×10^{-9} S/cm and 1×10^{-6} S/cm for BC5FO-AP and BC10FO-AP, respectively (Fig. 9). This clearly demonstrates an enhancement in the photoconductivity response with increasing concentration of Ca^{2+} at Bi^{3+} site. An increase in oxygen vacancies with increasing Ca^{2+} content and a subsequent reduction in resistance are accounted to be the cause for the observed increase in photoconductivity response of doped AP samples. On the other hand, all the AA samples were highly resistive and showed a minimum photoresponse on illumination. The change in conductivity for BC5FO-AA on illumination is $\sim 4 \times 10^{-11}$ S/cm which is two orders of magnitude lower than that of BC5FO-AP. For BC10FO-AA, this is found to be four orders lesser compared to BC10FO-AP with the change in conductivity $\sim 10^{-10}$ S/cm.

For an ideal semiconductor, carrier generation and recombination lifetimes are the same because photocurrent involves electron transfer only between the valance band and the conduction band. However, different generation and recombination lifetimes suggest that the mechanism of photocurrent is not a simple band to band excitation mechanism, but it involves (shallow) trap levels that capture and re-emit charges according to their time constant.[35] The trap states arise due to localized defects (vacancies and substitutions) and imperfections in the lattice. The effective generation and recombination lifetime can be determined by fitting the experimental data with the exponential equation. Rising and decreasing parts of conductivity curves are fitted with equations to understand the relaxation behavior of carrier generation and recombination. Figure 10 shows the fitted curves with original data for all AP and AA samples. By fitting the rising part of the conductivity using the exponential equation $\frac{\sigma_t - \sigma_{off}}{\sigma_{on} - \sigma_{off}} = \frac{\Delta\sigma_t}{\Delta\sigma_{total}} = a\left(1 - e^{-\frac{t}{\tau_g}}\right)$, where $\Delta\sigma_t$ $(=\sigma_t - \sigma_{off})$ is the difference in conductivity at any time (σ_t) with respect to OFF condition (σ_{off}), $\Delta\sigma_{total}$ $(=\sigma_{on} - \sigma_{off})$ is the difference in conductivity between the ON (σ_{on}) and OFF (σ_{off}) states, and a is a constant, average carrier generation lifetime (τ_g) is found. The decreasing part of conductivity is fitted using a stretched exponential function $\frac{\sigma_t - \sigma_{off}}{\sigma_{on} - \sigma_{off}} = \frac{\Delta\sigma_t}{\Delta\sigma_{total}} = a\, e^{-\left(\frac{t}{\tau_r}\right)^b}$, where τ_r is carrier recombination lifetime, a is a constant, and b indicates the deviation from the exponential function. But BFO-AA showed a reverse trend in photoconductivity. Only for this sample, decreasing part of the conductivity in ON state is fitted with $\frac{\sigma_t - \sigma_{on}}{\sigma_{off} - \sigma_{on}} = \frac{\Delta\sigma_t}{\Delta\sigma_{total}} = a\, e^{-\left(\frac{t}{\tau_t}\right)^b}$ where τ_t corresponds to the photoinduced trap generation lifetime.

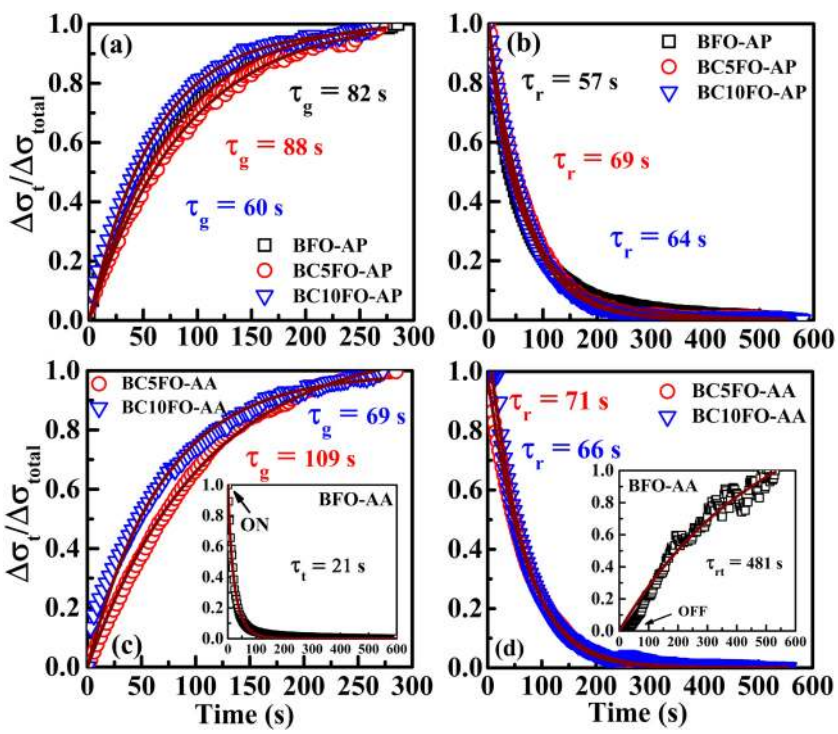

FIG. 10. The increasing and decreasing segments of [(a) and (b)] as-prepared (AP) and [(c) and (d)] air-annealed (AA) pellets of $Bi_{1-x}Ca_xFeO_{3-\delta}$ ($x = 0$, 0.05, and 0.1) during ON and OFF conditions of AM 1.5. Insets of [(c) and (d)] show the reverse trend of photoconductivity response in BFO-AA. Open symbols show the experimental response, and solid line is the exponential fit.

The increasing part of the conductivity in OFF state is fitted with the equation $\frac{\sigma_t-\sigma_{on}}{\sigma_{off}-\sigma_{on}} = \frac{\Delta\sigma_t}{\Delta\sigma_{total}} = a\left(1 - e^{-\frac{t}{\tau_{rt}}}\right)$, where τ_{rt} is the trapped charge carrier recovery time constant. All the fitted parameters are listed in Table III. Carrier recombination lifetimes are found to be between 57 s and 71 s for all AP pellets and AA pellets except for BFO-AA. This implies similar recombination relaxation behavior irrespective of defect concentration. More variation in the carrier generation lifetime with values ranging from ~70 s to 109 s is observed for all the AP and AA pellets excluding BFO-AA. BFO-AA showed a reverse trend in photoconductivity with photoinduced trap generation lifetime 21 s and trapped charge carrier recovery time constant 481 s.

B. Study of defect states from density functional calculations

Besides the experimental observation of defect state mediated photoconduction, a theoretical study is desirable to examine the robustness of experimental results as well as to develop a mechanism that explains the underlying physics. In this context, electronic structure calculations on BCFO are performed and further insight into the defect state formation and nature of electron transitions among these states is obtained.

1. Structural and computational details

We considered a fully relaxed rhombohedral distorted structure of $BiFeO_3$ (BFO) with space group R3c (161) having lattice parameters $a = 5.58$ Å and $c = 13.8$ Å.[36,37] A six formula unit BFO cell was used to examine bulk compound with defects. Similarly, a slab geometry (six formula unit BFO + 15 Å vacuum) was considered to study surface defect states. Along with the pristine BFO, the following six symmetry breaking configurations, I to VI as demonstrated in Fig. 11, were considered to study the defect states arising from O vacancies, Ca doping, and surface dangling obritals. (I) The O vacancy was created by removing one oxygen atom from the interior corresponding to a vacancy concentration of 5.5 at. %. (II) Pristine slab with no vacancies. (III) Two oxygen atoms were removed, one each from surface and interior to create a vacancy concentration of 11 at. %. (IV) Two Ca atoms were substituted at the Bi site (Ca_{Bi}) and one O atom was removed from the interior, but away from Ca_{Bi}. (V) With two Ca_{Bi}, two O atoms were removed, one close to Ca and the other away from it. (VI) In addition to the configuration of V, a surface O atom is removed. Though there are other inequivalent O atoms available, on the surface and in the interior, to create defect states, we have only focussed on few as they are sufficient to develop an understanding on the relation between photoconductivity and defect states.

The electronic structure calculations were performed by employing a pseudopotential based plane wave basis as implemented in Quantum Espresso package.[38] The generalized gradient approximation (GGA) with Perdew Burke-Ernzerhof (PBE)[39] was adopted for exchange-correlation functional. The onsite Coulomb interaction for Fe 3*d* electrons was included in the calculation using GGA + U approach with U = 5 eV.[40] All structures were relaxed in a $4 \times 4 \times 1$ Monkhorst Pack grid.[41] The cutoff for the kinetic energy was fixed to 50 Ry for the plane wave expansion of the electronic wave function. BFO is known to have a cycloidal (spiral) magnetic ordering with the cycloid length of 62 ± 2 nm.[42] However, on a closer look, each unit cell has a near G-AFM ordering and the reminiscent magnetic moment is responsible for the formation of spin cycloid. Since the objective in this work is restricted to examine the defect states, an ideal G-AFM ordering has been considered. Similar assumptions are made by others.[16,43,44]

2. Band structure of $Bi_{1-x}Ca_xFeO_{3-\delta}$

The band structures of $Bi_{1-x}Ca_xFeO_{3-\delta}$ for the aforementioned configurations, in G-AFM magnetic ordering, are shown in Fig. 11. The pristine BFO exhibits a bandgap of 2.65 eV, separating the O-*p* dominated valence bands and Fe-*d* dominated conduction bands which is in agreement with the previous theoretical and experimental studies.[16,45,46] The position of the Fe-*d* and O-*p* states is schematically illustrated in Fig. 12. The Fe-*d* states are occupied in one spin-channel and are empty in the other to satisfy d^5 configuration. For AFM arrangement, in one sublattice, the spin-majority channel is formed by spin-up states, and in the other sublattice, it is formed by spin-down states. With an oxygen vacancy in the bulk, one of the Fe^{3+}-O^{2-}-Fe^{3+} interaction is broken. As a consequence, the oxidation states of Fe ions (Fe1 and Fe2, see Fig. 12) in the vacancy neighbourhood are expected

TABLE III. Equations used to fit the photoresponse curves (as in Figs. 9 and 10) during the ON and OFF conditions along with the obtained fitted parameters are listed.

	Equations and fitted parameters	
	Light ON	Light OFF
Sample name	$\frac{\sigma_t-\sigma_{off}}{\sigma_{on}-\sigma_{off}} = \frac{\Delta\sigma_t}{\Delta\sigma_{total}} = a\left(1 - e^{-\frac{t}{\tau_g}}\right)$	$\frac{\sigma_t-\sigma_{off}}{\sigma_{on}-\sigma_{off}} = \frac{\Delta\sigma_t}{\Delta\sigma_{total}} = a\, e^{-\left(\frac{t}{\tau_r}\right)^b}$
BFO-AP	$a = 1.01$, $\tau_g = 82.1$ s	$a = 1.046$, $\tau_r = 57.2$ s, $b = 0.77$
BC5FO-AP	$a = 1.02$, $\tau_g = 87.7$ s	$a = 0.99$, $\tau_r = 69.5$ s, $b = 1$
BC5FO-AA	$a = 1.01$, $\tau_g = 109$ s	$a = 0.98$, $\tau_r = 70.8$ s, b = 1.06
BC10FO-AP	$a = 0.98$, $\tau_g = 60$ s	$a = 0.98$, $\tau_r = 63.6$ s, $b = 0.98$
BC10FO-AA	$a = 0.99$, $\tau_g = 69.2$ s	$a = 0.92$, $\tau_r = 66$ s, b = 0.89
BFO-AA	$\frac{\sigma_t-\sigma_{on}}{\sigma_{off}-\sigma_{on}} = \frac{\Delta\sigma_t}{\Delta\sigma_{total}} = a\, e^{-\left(\frac{t}{\tau_t}\right)^b}$ $a = 1.04$, $\tau_t = 21.6$ s, $b = 0.84$	$\frac{\sigma_t-\sigma_{on}}{\sigma_{off}-\sigma_{on}} = \frac{\Delta\sigma_t}{\Delta\sigma_{total}} = a\left(1 - e^{-\frac{t}{\tau_{rt}}}\right)$ $a = 1.483$, $\tau_{rt} = 481.6$ s

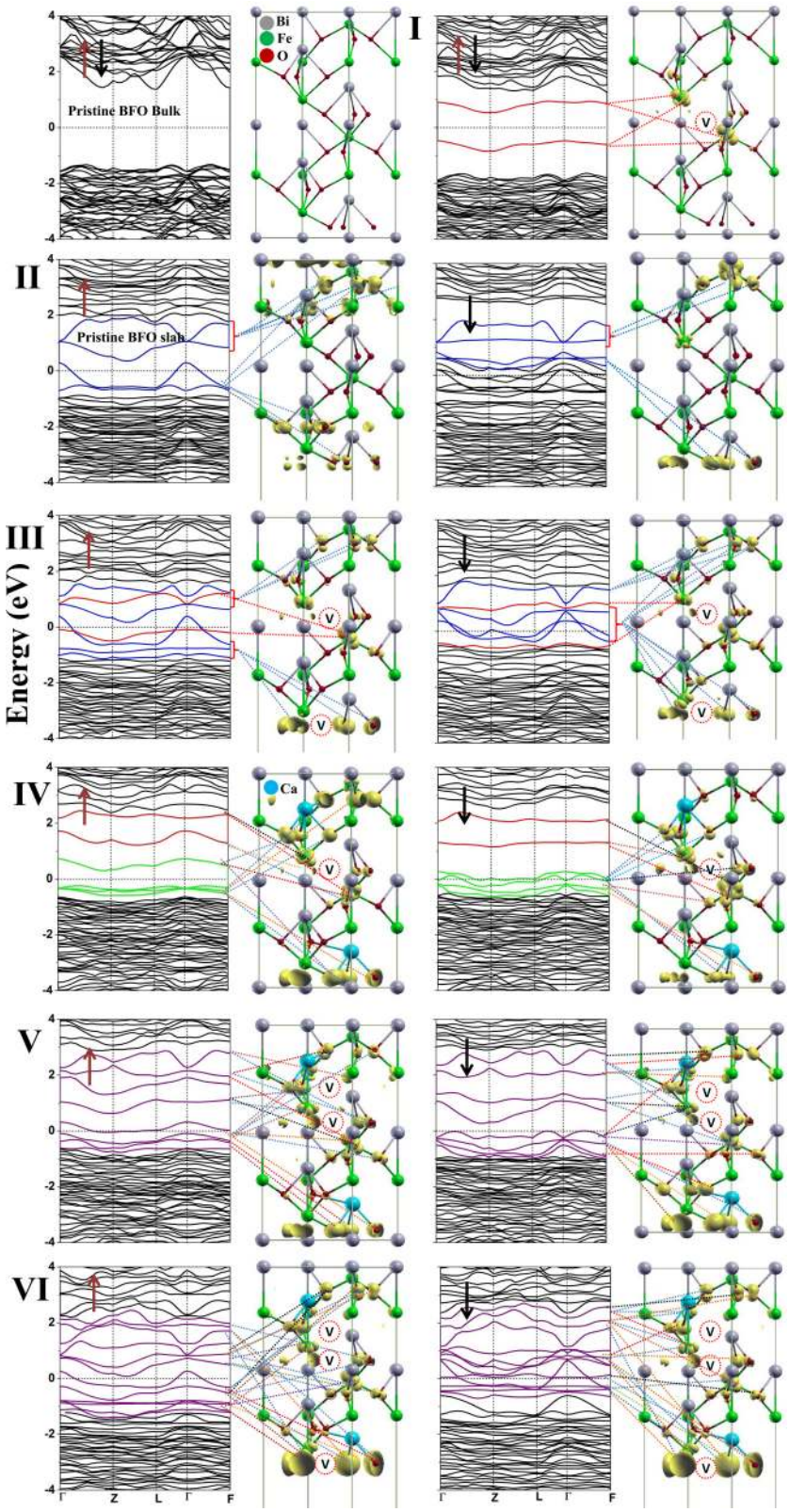

FIG. 11. Band structures for pristine BFO (top left), (I) Interior oxygen vacancy (top right), (II) Pristine slab indicating the dangling states, (III) Interior and surface oxygen vacancy, (IV) Ca doping with Interior oxygen vacancy, (V) Ca doping with one O_V near Ca and other away from Ca, (VI) Same as V, but with an additional O_V at the surface. The defect states are indicated in colours, and the spatial distribution of these defect states is shown through the iso-surface charge densities. Red represents the defect states coming from interior vacancies. Blue represents the states arising from the dangling bands and surface vacancies. Green denotes the defects states affected by Ca doping. However, with increasing vacancies (configurations V and VI) these states, as indicated in purple, intermix and spread over the whole sample. The spin-up and spin-down bands are indicated through up and down arrows, respectively.

to decrease from +3 to +2 leading to a d^6 configuration. This implies that in the high spin state, one of the spin-minority states (for both Fe1 and Fe2) will be occupied. Therefore, under ideal condition, the net local magnetic moment of Fe1 or Fe2 will decrease by 1 μ_B. However, these spin-minority states interact with the existing O-p states in the same spin channel to create one bonding defect state below the Fermi level (E_F) and one anti-bonding defect state above E_F [the red bands of Fig. 11(I)]. The charge densities corresponding to these defect bands confirm the hybridization between Fe-d and O-p states around the vacancy. The process is schematically illustrated in Fig. 12. As a result, there is a significant induced magnetic moment, of the order of 0.15 μ_B at the neighbouring oxygen sites. We find that with d^5 configuration the Fe moment is 4.3 μ_B and with a vacancy around, the moment reduces to 3.9 μ_B.

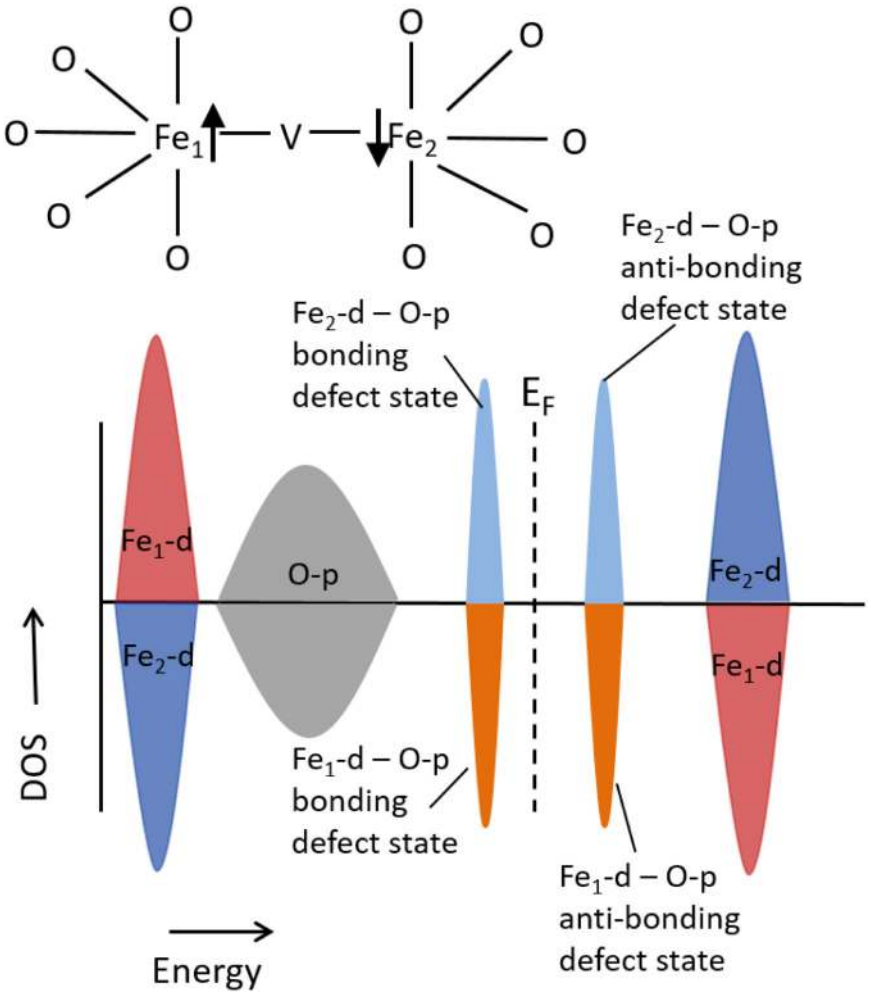

FIG. 12. Schematic representation of the formation of bonding and antibonding defect states in the presence of an oxygen vacancy. The bulk Fe-d and O-p DOS in the antiferromagnetic configurations are also shown.

The second configuration shows the defect states arising from the surface dangling bands which are shown in blue. In the third configuration, we considered the formation of two vacancies, one at the surface and other in the interior. The resultant electronic structure for both the spin-channel is shown in Fig. 11 (configuration III). Here, the doubly degenerate red bands are the defect states that arose due to the interior vacancy which resembles that of the bulk defect states (configuration I). The blue bands are the defect states arose due to the surface vacancy, surface dangling states, and broken Fe-O bonds. Therefore, with reduced symmetry, the surface defect states are non-degenerate. Also in this configuration, the spin-up and spin-down states differ in energy to double the non-degeneracy. As a consequence, unlike the case of two transition probable states in bulk BFO with vacancies, the present configuration creates ten transition probable states, with closer energy intervals, within the pristine bandgap.

When the bulk system is doped with charge compensating Ca atoms at Bi site and has oxygen vacancies, the electronic structure of the system can be explained from Fig. 11 (configuration IV). It shows that the bonding defect states (the lower red bands in both the spin-channel), which were occupied in the absence of Ca dopants, are now unoccupied suggesting that the Fe atoms around the vacancy are in 3+ charge state with d^5 configuration. The electrons donated by the bonding defect states are now redistributed among the oxygen anions to form O-p defect bands (shown in green). Therefore, like the configuration with surface vacancies [Fig. 11 (configuration III)], Ca doping increases the number of transition probable states. Further increase in bulk vacancies, as in configuration V, and an increase in interior as well as surface vacancies as in configuration VI increase the number of defect states. These states interact among each other to create defect bands (shown in purple). These bands are responsible for diffuse absorption edge as observed experimentally (Fig. S4 in the supplementary material). We further note that the BCFO not necessarily maintains the antiferromagnetic ordering. For configurations V and VI, we find an uncompensated magnetic moment of 0.5 and 1.5 μ_B, respectively. Experimentally, it is found that an increase in Ca doping concentration leads to enhanced magnetization in $BiFeO_3$.[47]

C. Mechanism of photoconduction

Based on the above experimental and theoretical study, we propose a mechanism for photoconductivity in pure BFO and Ca-doped BFO SPS pellets. Oxygen vacancies on the surface of nanoparticles residing along the grain boundaries were proposed to create defect states as shown in the band structure of Fig. 11 (configuration III). Here, defect states with close energy intervals generate photoconductivity

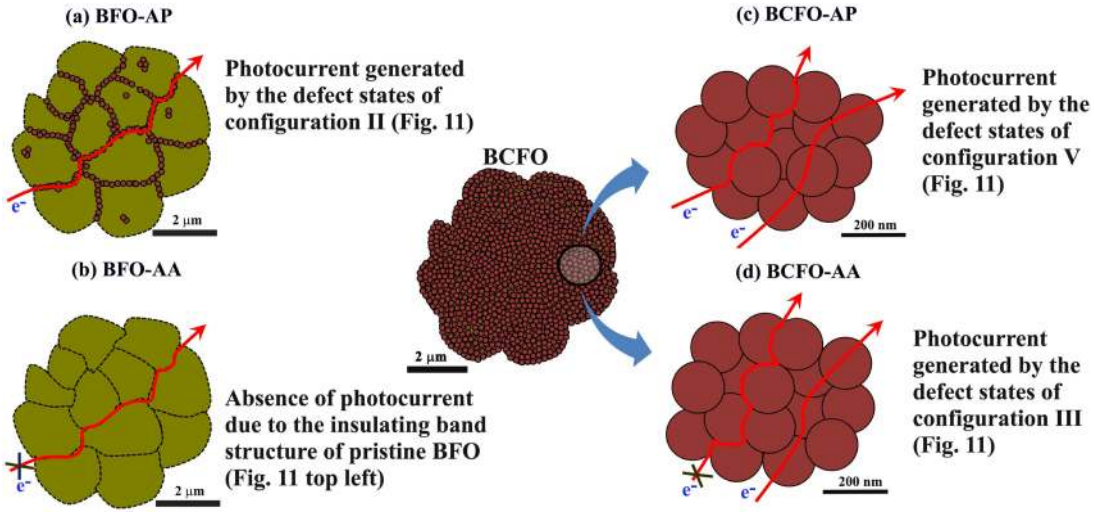

FIG. 13. Schematic of microstructural morphologies found in (a) BFO-AP, (b) BFO-AA, (c) BCFO-AP, and (d) BCFO-AA SPS pellets. The corresponding band structures that best represent the material are indicated in the text next to the schematic figure. The dense defect states produced from surface oxygen vacancies (O_V) of the nanoparticles at the grain boundaries (as in BFO-AP and BCFO-AP) provide conducting channel for e^- (marked by red lines). O_V created by Ca doping inside the grain (bulk-O_V) also produce dense defect levels (as in BCFO-AP and BCFO-AA) for photoconduction. In the case of BCFO-AA grain boundary, O_V defect states are suppressed due to air annealing, whereas bulk-O_V present within the bulk due to Ca doping are shown to survive.

response. This plays a crucial role in photoconduction in BFO-AP pellet [refer to the schematic in Fig. 13(a)]. In the absence of oxygen vacancies at grain boundaries, the photoconduction was shown to be poor and the photoconductivity decreases due to the trapping of electrons at photoinduced deep states in pure BFO.[23] The absence of photoconductivity in BFO-AA can be inferred from the insulating band structure of pristine BFO as shown in Fig. 11 (top left). It is important to note that the nanoparticles (100 to 200 nm) residing at grain boundaries contribute more to the total photoconductivity than the bulk grains. With Ca doping in BFO (BC5FO and BC10FO), the grain sizes are mostly limited to be around 100 to 200 nm, which is comparable to the size of nanoparticles residing at the grain boundaries in BFO-AP pellet (refer to Fig. 13 schematic). The fact that the surface is more disordered than the nanoparticle-core suggests that a significant fraction of oxygen vacancies are present at the grain boundaries in BCFO samples and contribute for the photoconductivity [Fig. 13(c)]. The corresponding band structure resembles Fig. 11 (configuration VI) where a well-dispersed and dense defect band enhances the photoconductivity. The photoconductivity increases with an increase in Ca^{2+} content in BCFO and is found to be two to four orders of magnitude large compared to that of BFO-AP. This distinctly shows the role of O_V created by the Ca doping on the photoconductivity. On air-annealing, the surface vacancies and excess vacancies in the interior are suppressed. The corresponding band structure resembles Fig. 11 (configuration IV). Here, the photoconductivity mainly takes place through the conduction channels provided by the bulk-O_V states, i.e., the conduction through the grain boundaries becomes negligible [Fig. 13(d)]. Despite the presence of Ca^{2+} in BCFO-AA, the magnitude of photoconductivity is similar to that observed in BFO-AP without Ca^{2+}. This implies that oxygen vacancies resulting from both the bulk and nanoparticle surfaces are important for the photoconductivity response. Three orders of difference in photoconductivity response between BCFO-AP and BCFO-AA confirm the dominant role played by the grain boundary defects than the bulk defects. All these studies suggest that the photoconductivity can be tailored by controlling the defect structure at the grain and grain boundaries.

IV. CONCLUSION

In conclusion, spark plasma sintered pure BFO and Ca doped $BiFeO_3$ ceramics with nanocrystalline grains were fabricated and their photoconductivity response is reported. It is shown that the grain boundary photoconductivity is dominant in both as-prepared samples of BFO and BCFO with the latter showing larger conductivity. With Ca^{2+} doping, the O_V concentration increases to favor the charge compensation. The defect states arising from oxygen vacancies residing at the surface of nanoparticles are shown to largely contribute for the photoconductivity. The experimental observations are validated from density functional theory calculations. Based on the results and analysis, we propose a mechanism, schematically illustrated in Fig. 13, that explains the large scale enhancement in photoconductivity in calcium doped bismuth ferrite. Dense defect states resulting from the surface oxygen vacancies form a band which occupies the pristine bandgap. As a consequence, there is diffuse band edge absorption which enhances the photoconductivity response. These studies suggest that for solar cell device application, in addition to optimizing the composition, more emphasis is to be given on tailoring the microstructural features to achieve large short circuit current.

SUPPLEMENTARY MATERIAL

Supplementary material includes (i) temperature dependent (303 K to 573 K) Nyquist plots and bode plots, (ii)

Gaussian profiles fitting of bode plots, and (iii) Tauc plot of SPS pellets.

ACKNOWLEDGMENTS

C.S. acknowledges the support from DST-SERB through Grant No. EMR/2016/002785 and the support from DST-SERI through Grant No. DST/TM/SERI/2K11/113. B.R.K.N acknowledges the support by DST, India, through Grant No. EMR/2016/003791 for the theoretical part of this work. K.K. would like to thank DST-SERB for providing financial support under NPDF scheme.

[1]G. Catalan and J. F. Scott, Adv. Mater. **21**(24), 2463–2485 (2009).
[2]M. Kianinia, K. Ahadi, and A. Nemati, Mater. Lett. **65**(19), 3086–3088 (2011).
[3]T. Choi, S. Lee, Y. J. Choi, V. Kiryukhin, and S.-W. Cheong, Science **324**(5923), 63–66 (2009).
[4]M. Yang, A. Bhatnagar, Z. Luo, and M. Alexe, Sci. Rep. **7**, 43070 (2017).
[5]A. Bhatnagar, A. Roy Chaudhuri, Y. Heon Kim, D. Hesse, and M. Alexe, Nat. Commun. **4**, 2835 (2013).
[6]B. Ramachandran, A. Dixit, R. Naik, G. Lawes, and M. S. R. Rao, Phys. Rev. B **82**(1), 012102 (2010).
[7]S. Li, Y.-H. Lin, B.-P. Zhang, Y. Wang, and C.-W. Nan, J. Phys. Chem. C **114**(7), 2903–2908 (2010).
[8]P. Mocherla, C. Karthik, R. Ubic, M. S. Rao, and C. Sudakar, Appl. Phys. Lett. **103**(2), 022910 (2013).
[9]D. C. Arnold, K. S. Knight, G. Catalan, S. A. T. Redfern, J. F. Scott, P. Lightfoot, and F. D. Morrison, Adv. Funct. Mater. **20**(13), 2116–2123 (2010).
[10]T. R. Paudel, S. S. Jaswal, and E. Y. Tsymbal, Phys. Rev. B **85**(10), 104409 (2012).
[11]T.-J. Park, G. C. Papaefthymiou, A. J. Viescas, A. R. Moodenbaugh, and S. S. Wong, Nano Lett. **7**(3), 766–772 (2007).
[12]S. M. Selbach, T. Tybell, M.-A. Einarsrud, and T. Grande, Chem. Mater. **19**(26), 6478–6484 (2007).
[13]S. Goswami, D. Bhattacharya, and P. Choudhury, J. Appl. Phys. **109**(7), 07D737 (2011).
[14]P. Chen, X. Xu, C. Koenigsmann, A. C. Santulli, S. S. Wong, and J. L. Musfeldt, Nano Lett. **10**(11), 4526–4532 (2010).
[15]J. Dho, X. Qi, H. Kim, J. L. MacManus-Driscoll, and M. G. Blamire, Adv. Mater. **18**(11), 1445–1448 (2006).
[16]S. J. Clark and J. Robertson, Appl. Phys. Lett. **90**(13), 132903 (2007).
[17]S. V. M. Pavana, G. Sanjeev, C. Keun Hwa, M. S. R. Rao, and C. Sudakar, Mater. Res. Exp. **2**(9), 095012 (2015).
[18]P. Mocherla, C. Karthik, R. Ubic, M. S. Rao, and C. Sudakar, Appl. Phys. Lett. **105**(13), 132409 (2014).
[19]K. K. Bharathi, W.-M. Lee, J. Sung, J. Soo Lim, S. Jin Kim, K. Chu, J. Won Park, J. Song, M.-H. Jo, and C.-H. Yang, Appl. Phys. Lett. **102**(1), 012908 (2013).
[20]N. Maso, H. Beltran, M. Prades, E. Cordoncillo, and A. R. West, Phys. Chem. Chem. Phys. **16**(36), 19408–19416 (2014).
[21]N. Masó and A. R. West, Chem. Mater. **24**(11), 2127–2132 (2012).
[22]R. L. Gao, C. L. Fu, W. Cai, G. Chen, X. L. Deng, H. W. Yang, J. R. Sun, Y. G. Zhao, and B. G. Shen, Mater. Res. Exp. **1**(3), 035016 (2014).
[23]S. Nandy, P. Mocherla, and C. Sudakar, J. Appl. Phys. **121**(20), 203102 (2017).
[24]R. Haumont, P. Bouvier, A. Pashkin, K. Rabia, S. Frank, B. Dkhil, W. A. Crichton, C. A. Kuntscher, and J. Kreisel, Phys. Rev. B **79**(18), 184110 (2009).
[25]R. Palai, H. Schmid, J. F. Scott, and R. Katiyar, Phys. Rev. B **81**(6), 064110 (2010).
[26]J. Allibe, K. Robin, E. Jacquet, I. Infante, S. Fusil, C. Carrétéro, J.-L. Reverchon, B. Marcilhac, D. Créte, J. C. Mage, A. Barthelemy, and M. Bibes, Appl. Phys. Lett. **96**(18), 182902 (2010).
[27]P. Hermet, M. Goffinet, J. Kreisel, and P. Ghosez, Phys. Rev. B **75**(22), 220102 (2007).
[28]P. Suresh and S. Srinath, J. Appl. Phys. **115**(17), 17D905 (2014).
[29]K. Pawan, P. Chandrakanta, and K. Manoranjan, Smart Mater. Struct. **24**(4), 045028 (2015).
[30]T. Patri, S. K. Mandal, and A. Chandra, J. Appl. Phys. **116**(24), 244105 (2014).
[31]K. Min, F. Huang, Y. Jin, W. Zhu, and J. Zhu, Ferroelectrics **450**(1), 42–48 (2013).
[32]S. Steinsvik, R. Bugge, J. O. N. GjØNnes, J. TaftØ, and T. Norby, J. Phys. Chem. Solids **58**(6), 969–976 (1997).
[33]B. Kang, S. K. Choi, and C. H. Park, J. Appl. Phys. **94**(3), 1904–1911 (2003).
[34]C. S. Tu, C.-M. Hung, Z.-R. Xu, V. H. Schmidt, Y. Ting, R. R. Chien, Y.-T. Peng, and J. Anthoninappen, J. Appl. Phys. **114**(12), 124105 (2013).
[35]M. Alexe, Nano Lett. **12**(5), 2193–2198 (2012).
[36]F. Kubel and H. Schmid, Acta Crystallogr. B **46**(6), 698–702 (1990).
[37]C. Michel, J.-M. Moreau, G. D. Achenbach, R. Gerson, and W. J. James, Solid State Commun. **7**(9), 701–704 (1969).
[38]G. Paolo, B. Stefano, B. Nicola, C. Matteo, C. Roberto, C. Carlo, C. Davide, L. C. Guido, C. Matteo, D. Ismaila, C. Andrea Dal, G. Stefano de, F. Stefano, F. Guido, G. Ralph, G. Uwe, G. Christos, K. Anton, L. Michele, M.-S. Layla, M. Nicola, M. Francesco, M. Riccardo, P. Stefano, P. Alfredo, P. Lorenzo, S. Carlo, S. Sandro, S. Gabriele, P. S. Ari, S. Alexander, U. Paolo, and M. W. Renata, J. Phys. Condens. Matter **21**(39), 395502 (2009).
[39]J. P. Perdew, J. A. Chevary, S. H. Vosko, K. A. Jackson, M. R. Pederson, D. J. Singh, and C. Fiolhais, Phys. Rev. B **46**(11), 6671–6687 (1992).
[40]A. I. Liechtenstein, V. I. Anisimov, and J. Zaanen, Phys. Rev. B **52**(8), R5467–R5470 (1995).
[41]H. J. Monkhorst and J. D. Pack, Phys. Rev. B **13**(12), 5188–5192 (1976).
[42]I. Sosnowska and A. K. Zvezdin, J. Magn. Magn. Mater. **140–144**, 167–168 (1995).
[43]T. Shimada, T. Matsui, T. Xu, K. Arisue, Y. Zhang, J. Wang, and T. Kitamura, Phys. Rev. B **93**(17), 174107 (2016).
[44]S. Ju and T.-Y. Cai, Appl. Phys. Lett. **95**(23), 231906 (2009).
[45]T. Kanai, S.-i. Ohkoshi, and K. Hashimoto, J. Phys. Chem. Solids **64**(3), 391–397 (2003).
[46]F. Gao, Y. Yuan, K. F. Wang, X. Y. Chen, F. Chen, J.-M. Liu, and Z. F. Ren, Appl. Phys. Lett. **89**(10), 102506 (2006).
[47]P. S. V. Mocherla, D. Prabhu, M. B. Sahana, N. Y. Hebalkar, R. Gopalan, M. S. R. Rao, and C. Sudakar, J. Appl. Phys. **124**(7), 073904 (2018).